JACS
JOURNAL OF THE AMERICAN CHEMICAL SOCIETY
pubs.acs.org/JACS
Article

Fluorescence-Detected Mid-Infrared Photothermal Microscopy

Yi Zhang,[§] Haonan Zong,[§] Cheng Zong, Yuying Tan, Meng Zhang, Yuewei Zhan, and Ji-Xin Cheng*

Cite This: J. Am. Chem. Soc. 2021, 143, 11490−11499
Read Online
ACCESS | Metrics & More | Article Recommendations | Supporting Information

ABSTRACT: Mid-infrared photothermal microscopy is a new chemical imaging technology in which a visible beam senses the photothermal effect induced by a pulsed infrared laser. This technology provides infrared spectroscopic information at submicrometer spatial resolution and enables infrared spectroscopy and imaging of living cells and organisms. Yet, current mid-infrared photothermal imaging sensitivity suffers from a weak dependence of scattering on the temperature, and the image quality is vulnerable to the speckles caused by scattering. Here, we present a novel version of mid-infrared photothermal microscopy in which thermosensitive fluorescent probes are harnessed to sense the mid-infrared photothermal effect. The fluorescence intensity can be modulated at the level of 1% per Kelvin, which is 100 times larger than the modulation of scattering intensity. In addition, fluorescence emission is free of interference, thus much improving the image quality. Moreover, fluorophores can target specific organelles or biomolecules, thus augmenting the specificity of photothermal imaging. Spectral fidelity is confirmed through fingerprinting a single bacterium. Finally, the photobleaching issue is successfully addressed through the development of a wide-field fluorescence-detected mid-infrared photothermal microscope which allows video rate bond-selective imaging of biological specimens.

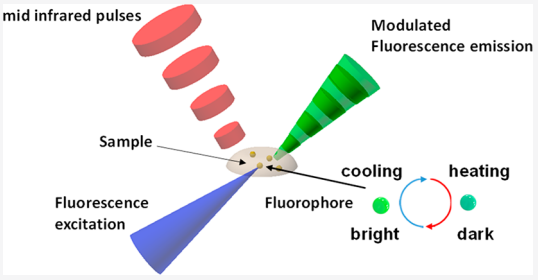

INTRODUCTION

Visualizing the molecular composition and monitoring the molecular dynamics in a complex living system is a central theme of life science. Fluorescence microscopy has been widely adopted in biomedical research as it provides high-speed background-free imaging with exquisite molecular specificity[1,2] and superior resolution reaching the nanometer scale.[3−5] While fluorescence microscopy excels at mapping the distribution and dynamics of tagged organelles such as mitochondria and biomolecules such as glucose[6] and cholesterol,[7] it does not provide chemical information on the tagged cells or organelles. Lacking such information hinders functional analysis, such as assessment of cell metabolic activity.

Providing chemical specificity, high-speed and high-sensitivity vibrational spectroscopic imaging is an emerging platform.[8] Recently developed coherent Raman scattering microscopy, based on coherent anti-Stokes Raman scattering (CARS) or stimulated Raman scattering (SRS), has allowed real-time vibrational imaging of biomolecules in living cells and tissues.[9,10] Advanced instrumentation has pushed the stimulated Raman spectral acquisition speed to the microsecond scale.[11] Adoption of stable isotope probes and alkyne-based Raman tags greatly enhanced the detection sensitivity, specificity, and functionality in SRS microscopy.[10] Being highly sensitive to C−H vibrations, CARS and SRS imaging have unveiled new signatures of lipid metabolism in a variety of biological systems.[12−14] In comparison, high-speed CARS or SRS imaging of fingerprint Raman bands remains difficult.

Mid-infrared spectroscopy is complementary to Raman spectroscopy. Unlike Raman scattering, the infrared absorption cross section in the fingerprint region is larger than that in the high-wavenumber C−H vibrational region. Fourier transform infrared (FTIR) spectroscopy is one of the most extensively used techniques for chemical characterization and analysis of biological cells and tissues.[15−18] The inherent vibration absorption of mid-infrared photons by biological macromolecules including proteins, lipids, carbohydrates, and nucleic acids shows distinctive absorption bands. Shifts in the relative heights of the absorption bands, peak positions, and peak shape provide rich biomolecular information, including the concentration, conformation, and orientation. FTIR spectroscopy has provided new insights in tissue classification,[19] drug and tissue interaction,[20] neurodegenerative diseases,[21] cancer progression,[22] and so on. However, the spatial resolution of infrared spectroscopic imaging is limited by the long mid-infrared illumination wavelength, ranging from 5 to 20 μm. Strong water absorption further hinders its application to living cells.

To overcome these limitations in infrared spectroscopy, a new platform, termed mid-infrared photothermal (MIP)

Received: April 6, 2021
Published: July 15, 2021

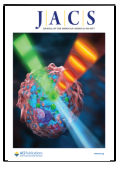

https://doi.org/10.1021/jacs.1c03642
J. Am. Chem. Soc. 2021, 143, 11490−11499

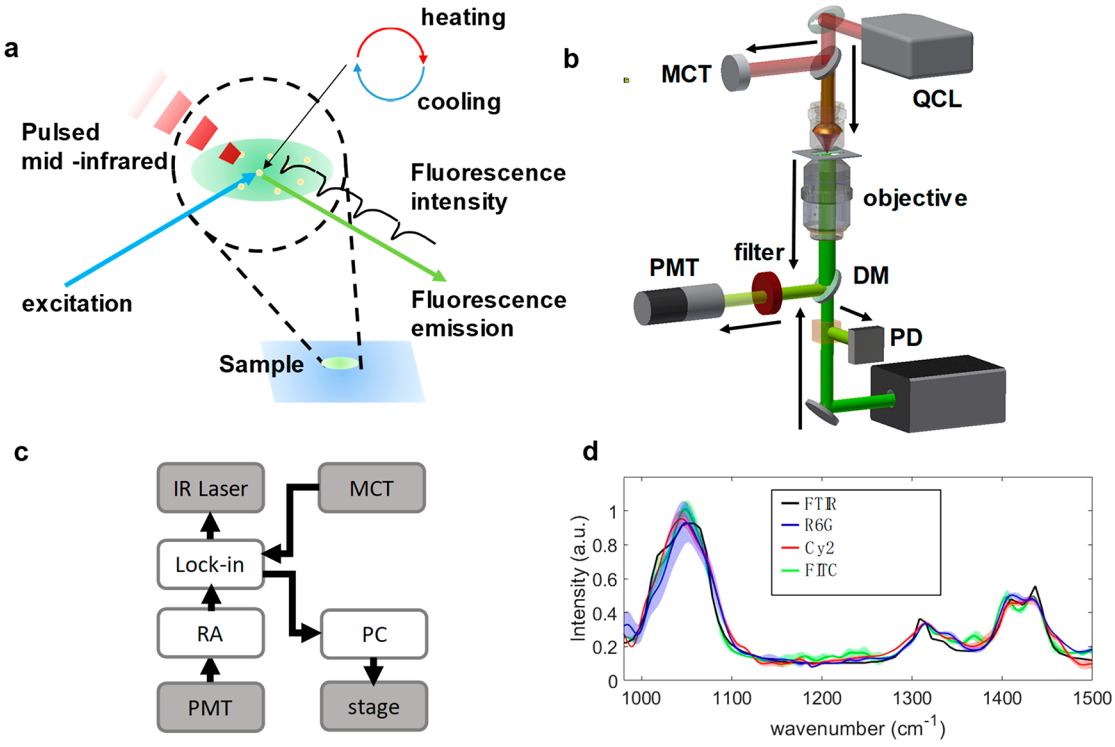

Figure 1. Fluorescence-detected mid-infrared photothermal (F-MIP) sensing principle, point-scanning microscope, and spectral fidelity. (a) Modulation of the fluorophore emission intensity by a pulsed infrared pump of surrounding molecules. (b) Schematic of a point-scanning F-MIP microscope. Pulsed mid-IR pump beam from a quantum cascade laser (QCL) and a continuous visible fluorescence excitation beam are focused at the sample with a reflective objective and a water-immersion objective, respectively. Fluorescence emission is reflected by a dichroic mirror (DM), filtered, and directed to a photomultiplier tube (PMT). Beam splitter is placed to reflect the scattered visible beam to a photodiode for scattering-based MIP (Sc-MIP) imaging. (c) Electronics connection. Pphotothermal signal is detected by a PMT connected to a resonant amplifier (RA) and detected by a lock-in amplifier. PC is used for controlling the scanning stage and data acquisition. (d) F-MIP spectra of DMSO supplemented with various thermosensitive fluorescent dyes. For each dye, the standard deviation of three independent measurements is shown at each wavenumber. FTIR spectrum of DMSO (black) is shown for comparison.

microscopy, has been developed recently[23−30] to reach submicrometer spatial resolution.[31] The MIP effect relies on a photothermal process in which infrared absorption corresponds to a specific molecular vibrational bond that causes a localized temperature rise in the vicinity of the target molecules. This photothermal effect consequently induces a change of refractive index and thermal expansion. The MIP signal is then obtained by probing these changes using a visible beam which provides a much smaller diffraction limit than the mid-infrared illumination, enabling a spatial resolution down to 300 nm.[30] Following the first demonstration of MIP imaging of living cells,[23] technical innovations have been made to enable MIP detection in wide field using scattering or phase signals.[32−35] Meanwhile, MIP microscopy and its commercial product have found various applications in studying living cells, pharmaceuticals, viruses, and bacteria.[25,27,28,36−40] Yet, the photothermal effect induces only a tiny change in the intensity and angular distribution of the scattered probe light due to the weak thermal dependence of the particle size and refractive index. Typical fractional change is on the order of $10^{-4}/K$, set by the intrinsic thermal properties of most materials. Such small modulation depth limits the signal-to-noise ratio (SNR), especially in the wide-field mode where the probe beam intensity at each pixel is limited by the well depth of a CMOS camera.[33]

Here, we report a fluorescence-detected MIP (F-MIP) microscope that utilizes thermosensitive fluorescent dyes as probes of the photothermal effect. The F-MIP principle is illustrated in Figure 1a. A sample stained with a thermosensitive dye is heated upon IR absorption by targeted molecules. The infrared pulse train heats the surrounding of the fluorescent probe and causes a temperature rise, which subsequently modulates the fluorescence emission efficiency. Such modulation is then measured by a lock-in amplifier. Using a fluorescent dye to measure the temperature has been performed.[41−44] Yet, it has not been used as a probe for infrared spectroscopic imaging. Our method offers a few key advantages over scattering-based MIP microscopy. The first is the utilization of a much larger photothermal response of fluorescent dyes compared to scattering. Common fluorophores including FITC, Cy2, Cy3, Rhodamine, and green fluorescent protein have temperature-dependent emission efficiencies on the order of $1\%/K$, which is nearly 100 times larger than the scattering dependence on temperature. Thus, one can in principle boost the mid-infrared photothermal imaging speed by 2 orders of magnitude. Second, as fluorescence appears at a new wavelength from the incident beam, it is insensitive to the laser relative intensity noise. Third, unlike scattering, fluorescence is incoherent and thus does not generate interference patterns. Finally, fluorescent probes can target specific cells, intracellular organelles, or specific molecules, thus offering an enhanced specificity beyond reach by scattering-based MIP microscopy. In this study, we report two F-MIP systems: one in point-scanning mode and one in wide-field mode, as detailed below.

https://doi.org/10.1021/jacs.1c03642
J. Am. Chem. Soc. 2021, 143, 11490−11499

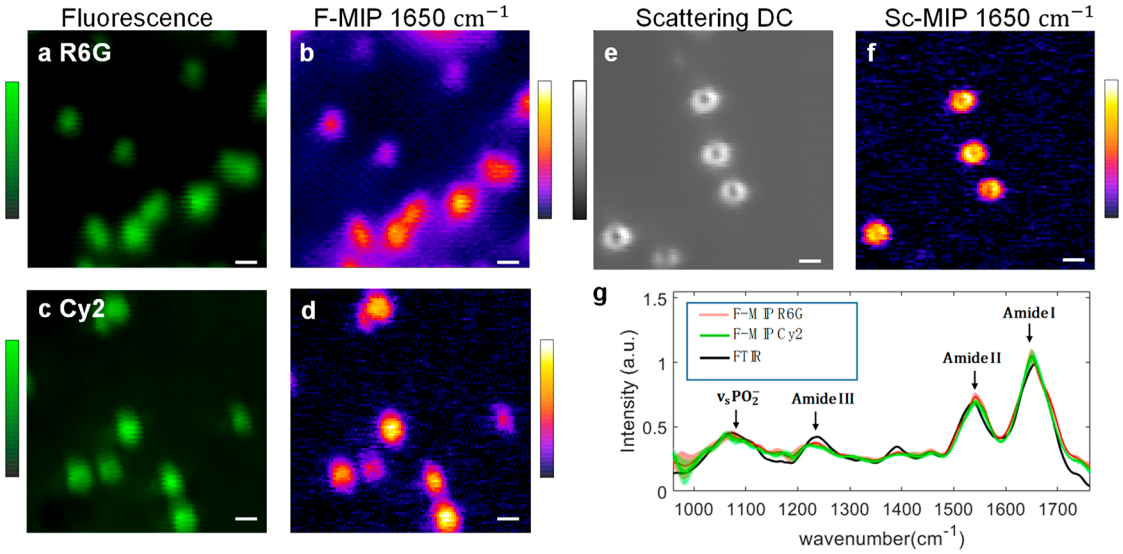

Figure 2. F-MIP imaging and fingerprinting single *S. aureus*. (a) Fluorescence image of *S. aureus* stained with R6G. Scale bar: 1 μm. Pixel dwell time: 1 ms. Fluorescence excitation: 0.025 mW at 532 nm. (b) F-MIP image of the same *S. aureus* at 1650 cm^{-1}. (c) Fluorescence image of *S. aureus* stained with Cy2. Fluorescence excitation: 0.025 mW at 488 nm. (d) F-MIP image of the same *S. aureus* at 1650 cm^{-1}. (e) Scattering image of *S. aureus*. Pixel dwell time: 1 ms. Visible probe power: 1.5 mW. (f) Sc-MIP image of the same *S. aureus* at 1650 cm^{-1}. (g) Fingerprint spectra of *S. aureus* measured by F-MIP and Sc-MIP, respectively. For both F-MIP and Sc-MIP, the IR laser power 1650 cm^{-1} was 10.2 mW at the sample. FTIR spectrum recorded from a film of dried *S. aureus* was adopted from ref 27. F-MIP imaging and fingerprinting of single bacteria.

EXPERIMENTAL SECTION

Scanning F-MIP Microscope. A pulsed mid-IR pump beam is generated by a tunable (from 1000 to 1886 cm^{-1}) quantum cascade laser (QCL, Daylight Solutions, MIRcat-2400) operating at a 100 kHz repetition rate and 900 ns pulse duration. The IR beam passes through a calcium fluoride (CaF_2) cover glass and is then focused onto a sample through a gold-coating reflective objective lens (52×; numerical aperture (NA), 0.65; Edmund Optics, 66589). A continuous-wave probe laser (Cobolt, Samba) at 532 nm is focused onto the same spot from the opposite side by a refractive objective (60×; NA, 1.2; water immersion; Olympus, UPlanSApo). The probe beam is aligned to be collinear to the mid-IR pump beam. The reflective objective is fine tuned in 3D to ensure overlap of the two foci. A scanning piezostage (Mad City Laboratories, Nano-Bio 2200) with a maximum scanning speed of 200 μs/pixel is used to scan the sample. The fluorescence is collected by the same refractive objective, reflected by a dichroic mirror (Thorlabs, DMSP550R, 550 nm cutoff), filtered by a long-pass filter (Thorlabs, FEL0550, 550 nm cutoff), and then collected by a PMT (Hamamatsu, H10721-110). Specimens on a CaF_2 coverglass are first imaged by fluorescence. Then, the pulsed IR laser is turned on and the modulated fluorescence signal is collected by the same PMT. The F-MIP signal is extracted by a lock-in amplifier (Zurich Instruments, HF2LI). A laboratory-built resonant circuit is used to amplify the photocurrent from the PMT before it is sent to the lock in. Before the reflective objective, the infrared laser passes through the CaF_2 slip and the reflected infrared laser intensity is measured by a mercury cadmium telluride (MCT) detector for normalization of IR power at each wavelength.

Wide-Field F-MIP Microscope. The IR pulses are generated by the same QCL used in scanning F-MIP. The visible probe beam for fluorescence excitation (wavelength at 488 or 520 nm) is obtained by second-harmonic generation of a quasi-continuous femtosecond laser tuned to 976 or 1040 nm (Coherent Inc., Chameleon, 140 fs, 80 MHz). Prior to second-harmonic generation, the femtosecond beam is chopped into a 200 kHz pulse train (300 ns pulse width) by an acousto-optical modulator (AOM, Gooch and Housego). The IR beam passes through the substrate and is weakly focused onto a sample by a parabolic mirror (f = 15 mm, Thorlabs, MPD00M9-M01). Using a Kohler illumination configuration, the probe beam is focused on the back focal plane of the objective lens (50×, 0.8 NA, Nikon) by a condenser (f = 75 mm, AC254-075-A, Thorlabs). The fluorescence emission is collected by the same objective lens and after a long-pass filter collected by a CMOS camera (FLIR, Grasshopper3 GS3-U3-51S5M). The F-MIP images are acquired by a virtual lock-in camera approach.[33] Briefly, a pulse generator (Emerald Pulse Generator, 9254-TZ50-US, Quantum Composers) generates a master clock signal at 200 kHz and externally triggers the QCL, the AOM, and the CMOS camera to synchronize the IR pump pulses, probe pulses, and camera exposure. The schematic is shown in Figure 4a.

Cancer Cell Culture and Staining. Mia Paca2 cells were purchased from the American Type Culture Collection (ATCC). The cells were cultured in RPMI 1640 medium supplemented with 10% FBS and 1% P/S. All cells were maintained at 37 °C in a humidified incubator with 5% CO_2 supply. For Nile Red staining, cells were incubated with 10 μM Nile Red (Invitrogen) for 30 min at room temperature followed by 15 min fixation in 10% neutral buffered formalin. For rhodamine 123 (Invitrogen) staining, cells were incubated with 10 μg/mL rhodamine 123 for 30 min at 37 °C.

Bacterial Culture and Staining. *Staphylococcus aureus* (*S. aureus*) was incubated in a MHB medium for 10 h. After centrifuging and washing in phosphate-buffered saline (PBS), the bacteria were fixed by formalin solution for 0.5 h. Rhodamine 6G or Cy2 at 10^{-4} M was then added into the bacteria pellet. The pellet was then resuspended and incubated for 1 h. With the final washing steps, 2 μL of the sample was dried on a CaF_2 coverslip for imaging. *Shigella flexneri* expressing GFP was grown overnight at 37 °C on a tryptic soy agar plate. Colonies with green fluorescence were picked up by sterile inoculation loops and then resuspended in PBS. The bacterial solution was diluted by optical density at 600 nm (OD600) to 0.1. The bacteria were then fixed by 10% formalin for 30 min at room temperature. The bacteria solution was washed twice by PBS before imaging.

RESULTS AND DISCUSSION

Point-Scanning F-MIP Microscope and Spectral Fidelity. On the basis of the principle shown in Figure 1a, we built a scanning F-MIP microscope as shown in Figure 1b. A QCL laser provides IR pulses tunable in the entire fingerprint region. The repetition rate and pulse width were set to 100 kHz and 900 ns, respectively. Two CW lasers at 532 and 488 nm were used for fluorescence excitation. The fluorescence was detected

https://doi.org/10.1021/jacs.1c03642
J. Am. Chem. Soc. 2021, 143, 11490−11499

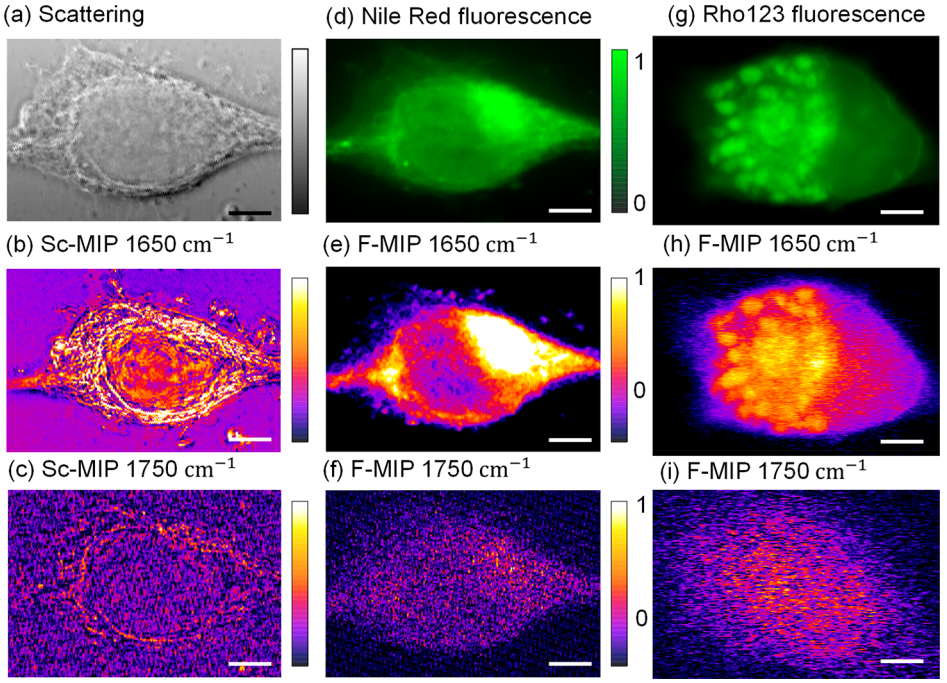

Figure 3. Sc-MIP and F-MIP images of living MiaPaca2 cancer cells. (a) Scattering image of a MiaPaca2 cell. (b) Sc-MIP image of the same cell at 1650 cm^{-1}. (c) Sc-MIP image at 1750 cm^{-1}. (d) Fluorescence image of the same MiaPaca2 cell stained with Nile red. Probe laser is at 532 nm. (e) F-MIP image at 1650 cm^{-1}. (f) F-MIP image at 1750 cm^{-1}. (g) Fluorescence image of a different MiaPaca2 cell stained with Rhodamine 123 (Rho123). Probe laser is at 488 nm. (h) F-MIP image at 1650 cm^{-1}. (i) F-MIP image at 1750 cm^{-1}. Scale bar: 5 μm. Sc-MIP and F-MIP imaging of cancer cells.

by a photomultiplier tube, and the F-MIP signal was extracted by a lock-in amplifier. On the same setup, a photodiode was also installed for scattering-based MIP (Sc-MIP) imaging using the 532 nm laser as the probe beam. The electronics connections are shown in Figure 1c.

Using this system, we validated the spectral fidelity of the F-MIP microscope. We dissolved various thermosensitive dyes in DMSO at 100 μM concentration. We then recorded the F-MIP signals while scanning the QCL laser. At each wavenumber, the F-MIP intensity was normalized by the IR intensity measured by MCT. In all cases (Figure 1d), the F-MIP spectra show the same peak intensity and width as the FITR spectrum of DMSO. Importantly, because the dye concentration (100 μM) is much lower than the DMSO concentration (14 M), the dyes do not interfere with the F-MIP spectra. These data demonstrate that the F-MIP microscope is able to produce reliable spectral information.

We applied the F-MIP microscope to image single *S. aureus* bacteria to evaluate its chemical imaging capability on biological specimens (Figure 2a–d). The *S. aureus* culture was diluted to a concentration of around 5×10^5/mL and then dried on a CaF_2 substrate. The *S. aureus* particles were stained with fluorescence dyes Cy2 and R6G. For each specimen, we acquired fluorescence and F-MIP images of the same bacteria at 1650 cm^{-1}, targeting the amide I band. For the F-MIP images, SNRs of 26 and 34 were achieved for R6G- and Cy2-labeled bacteria at a fluorescence excitation power of 0.025 mW at the sample. For comparison, we recorded scattering and MIP images of the same specimen (Figure 2e and 2f). In order to obtain a similar SNR of 37, an excitation power of 1.5 mW at the sample was required, which is 60 times the probe power used for F-MIP. On a single bacterium, we recorded the vibrational fingerprint spectrum (Figure 2g). The F-MIP spectra based on R6G and Cy2 match well with the FTIR spectrum, showing distinct peaks at 1650, 1550, and 1080 cm^{-1} for protein amide I, protein amide II, and nuclei acid phosphate vibrations, respectively. This comparison demonstrates the spectral fidelity of F-MIP in single-bacterium analysis. Notably, the scattering and the Sc-MIP image both show a ring structure with bright contrast from the peripheral of the cell (Figure 2e and 2f), whereas the F-MIP images (Figure 2b and 2d) show bright contrast from the entire cell. This result indicates that F-MIP is immune to edge-enhanced back scattering from a sizable particle.

Compared to bacteria, eukaryotic cells contain a nucleus and highly organized organelles in the cytoplasm. In the transmission image shown in Figure 3a, the scattering-based contrast shows the overall cell morphology. Accordingly, the Sc-MIP image (Figure 3b) at 1650 cm^{-1} corresponding to the amide I band shows the protein content inside the nucleus and protein-rich structures in the cytoplasm without specificity to a certain organelle. The contrast decreases when the IR laser is tuned to 1750 cm^{-1} (Figure 3c), showing the chemical specificity. In contrast, fluorescence microscopy is able to visualize specific biomolecules and/or intracellular organelles via the versatile fluorescent probes. For instance, Nile Red can selectively stain the intracellular lipid droplets and membranes,[45] while Rhodamine 123 is a specific probe for localizing mitochondria in living cells.[46] By staining the same cell with Nile Red and excitation of the dye at 532 nm, phospholipid membranes in the cell are visualized (Figure 3d), where the brightest contrast is likely from the ER membrane. The F-MIP image at 1650 cm^{-1} gives the distribution of proteins in areas labeled by Nile Red (Figure 3e). The contrast nearly disappears when the IR laser is tuned to 1750 cm^{-1} (Figure 3f), showing the chemical specificity. To show that our

https://doi.org/10.1021/jacs.1c03642
J. Am. Chem. Soc. 2021, 143, 11490−11499

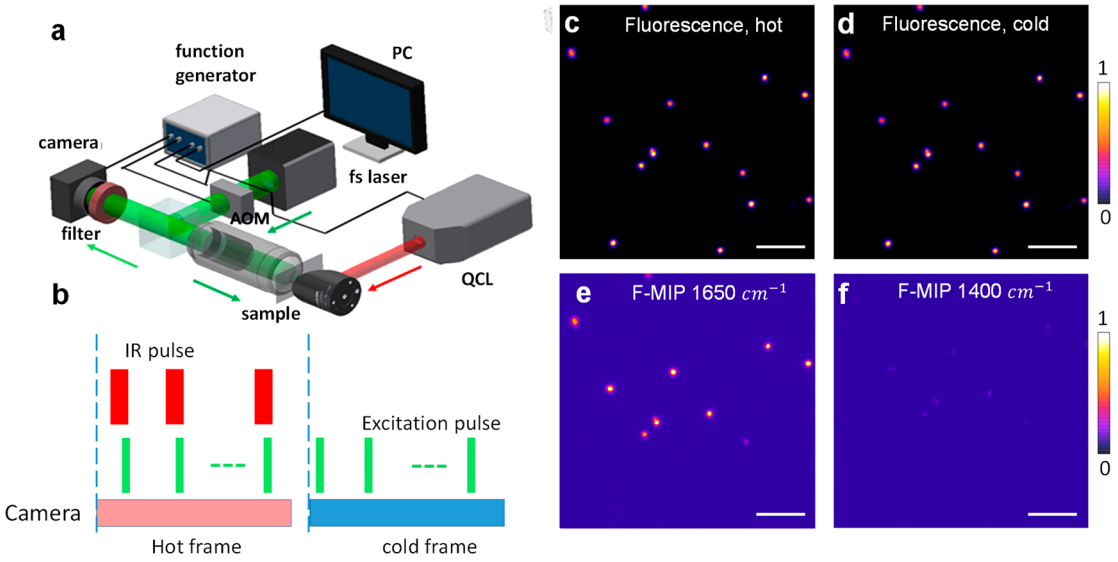

Figure 4. Wide-field F-MIP microscope. (a) Schematic of the wide-field F-MIP microscope. Infrared laser generated by the QCL is focused by a parabolic mirror. Visible light modulated by an AOM illuminates the sample and excites the fluorescence. Fluorescence is filtered and collected by a CMOS camera. (b) Temporal synchronization of the IR pump pulse, fluorescence excitation pulse, and camera exposure. (c, d) Wide-field fluorescence image of Cy2-stained *S. aureus* with IR on and IR off, designated as hot and cold, respectively. (e) Wide-field F-MIP at 1650 cm^{-1}. (f) F-MIP at 1400 cm^{-1} off resonance. Scale bar: 10 μm. Fluorescence excitation: 488 nm, 1 mW. IR pulse rate: 200 kHz. Camera frame rate: 40 Hz.

method is applicable to other dyes, we performed an independent experiment in which living MiaPaca2 cells were labeled by Rhodamine 123 targeting intracellular mitochondria (Figure 3g). In accordance, the F-MIP image at 1650 cm^{-1} shows selective and bright contrast from the Rhodamine 123-labeled region (Figure 3h) and the contrast disappears at 1750 cm^{-1} (Figure 3i).

From Point-Scanning to Wide-Field F-MIP. In the above experiments, the power used for F-MIP imaging is at the microwatt level and is 60 times less than the power used for scattering MIP imaging. The extremely low photon budget for F-MIP imaging opens the opportunity of increasing the throughput via wide-field illumination with IR pump pulses and visible probe pulses. Importantly, compared to scanning F-MIP, wide-field F-MIP could significantly reduce the fluorophore photobleaching rate based on the following consideration. In our experiment, the IR pulse is 900 ns in duration and the pulse-to-pulse duration is 10 μs. In the aqueous environment, the temperature profile largely follows the IR pulse. Thus, in a scanning experiment where a continuous wave probe laser is used, the duty cycle is about 10%. Yet, in a wide-field measurement, we only need two visible pulses to measure the IR-on and IR-off states. Thus, the duty cycle can be 50%. In this way, the probe laser power can be much reduced, thus alleviating the photobleaching issue. Notably, our group recently demonstrated scattering-based wide-field MIP imaging.[33] Yet, the signal-to-noise ratio at the high-speed mode is limited by the weak dependence of scattering on the temperature and the small well depth of the CMOS camera. As a result, a large number of integrations were needed to accumulate sufficient photons to probe the MIP signal. Unlike the scattering photons, the fluorescence usually does not saturate the camera. Due to the high thermosensitivity of fluorescent probes, it is anticipated that the MIP signal can be extracted from two sequential frames (hot and cold) without further averaging.

Wide-Field F-MIP Imaging System. On the basis of the above rationale, we built a wide-field F-MIP microscope as shown in Figure 4a. The pulsed infrared laser is weakly focused onto a sample by a parabolic mirror. An 80 MHz femtosecond laser is modulated by an AOM and frequency doubled to a visible window. The broad bandwidth of femtosecond pulses reduces speckles in scattering-based MIP imaging. The virtual lock-in detection scheme is illustrated in Figure 4b. The fluorescence excitation pulse is synchronized with the IR pump pulse. In the cold frame, no IR pump pulses heat the sample. The camera detects the hot and cold frames sequentially at 40 Hz frame rate. The difference (cold − hot) generates the MIP image. The average probe laser power was around 1 mW, and the exposure time was 300 ns. The IR power was in the range from 5 to 15 mW depending on the spectral window examined. To characterize the spatial resolution, we mapped Cy2-labeled polystyrene beads with a diameter of 500 nm; the F-MIP intensity profile shows a full-width at half maximum of 610 nm. After deconvolution with the particle size, the spatial resolution is estimated to be 390 nm, which is close to the diffraction limit of the 0.8 NA objective.

To demonstrate the applicability of wide-field F-MIP to biological specimens, we deposited *S. aureus* stained with Cy2 onto a silicon substrate and measured the fluorescence with IR-on and IR-off sequentially. The hot frame and the cold frame are illustrated in Figure 4c and 4d, respectively. By subtracting the hot from the cold frame, the intensity difference generates the F-MIP image shown in Figure 4e. When the IR laser is tuned to 1650 cm^{-1}, corresponding to the amide I band of the proteins, a signal-to-noise ratio of 30 was obtained. The IR pulse only heats the upper half of the field of view. For this reason, only the *S. aureus* particles in the upper part give the F-MIP contrast. When the IR laser is tuned to 1400 cm^{-1}, off resonance to major IR peaks, the contrast nearly disappears (Figure 4f). We note that the wide-field F-MIP imaging speed of 20 frames/s is 2000 times faster than the scanning F-MIP imaging speed (100 s per frame with a pixel dwell time of 1.0 ms).

Performance Comparison between Wide-Field Sc-MIP and F-MIP. Next, we compared the performance of

https://doi.org/10.1021/jacs.1c03642
J. Am. Chem. Soc. 2021, 143, 11490−11499

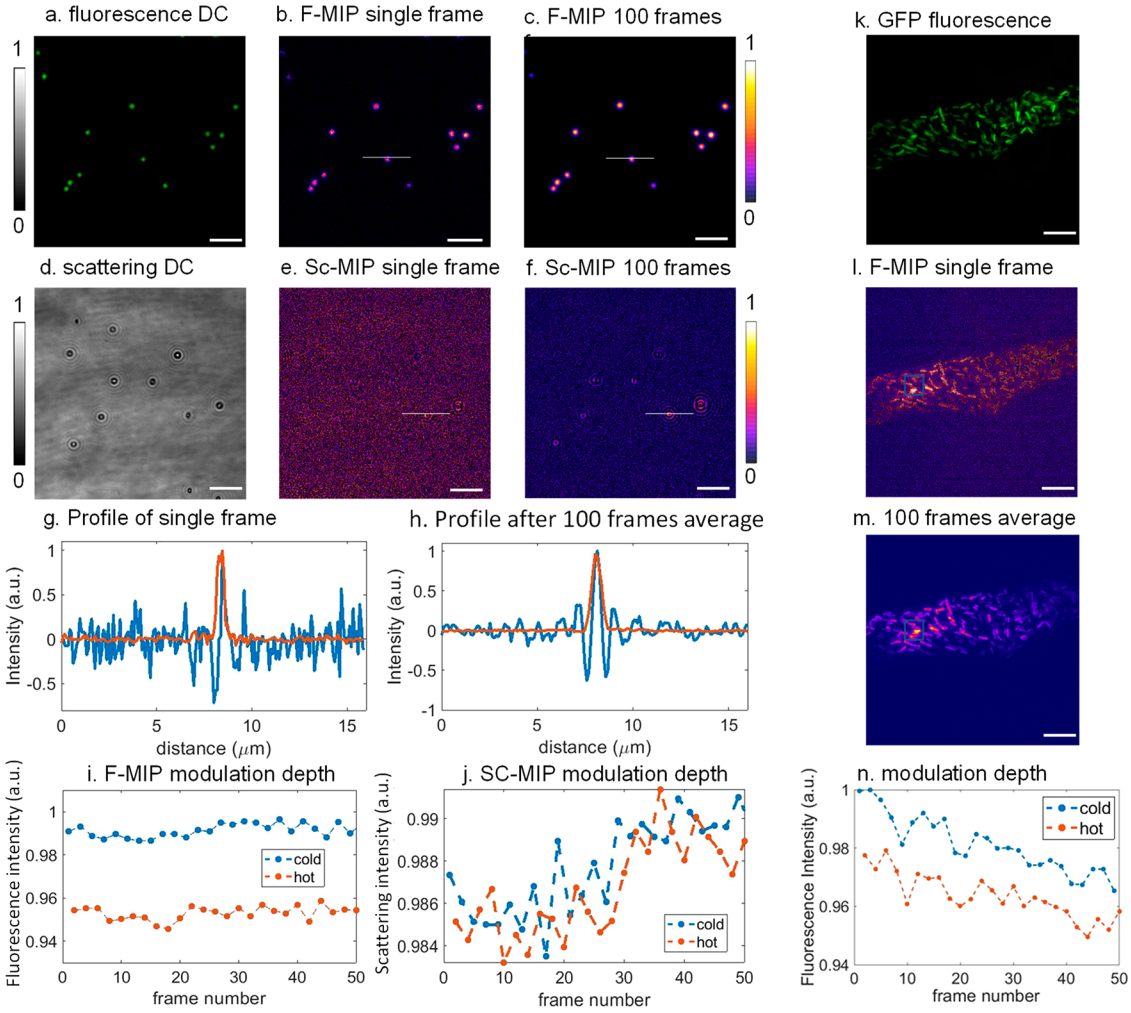

Figure 5. Performance comparison between wide-field SC-MIP and wide-field F-MIP systems. (a) Fluorescence image of *S. aureus* deposited on a silicon substrate. (b) Single-frame F-MIP image of the same cells at 20 Hz speed. (c) F-MIP image of the same cells with 100 frames average. (d) Scattering image of *S. aureus* deposited on a silicon substrate. (e) Single-frame Sc-MIP of the same cells shown in d at 20 Hz speed. (f) Sc-MIP of the same field of view with 100 frames average. (g) Intensity profile along the white line marked in b and e. (h) Intensity profile along the white line marked in c and f. (i) Fluorescence intensity of single *S. aureus* in sequentially acquired hot and cold frames. (j) Scattering intensity of single *S. aureus* in sequentially acquired hot and cold frames. IR laser is tuned to 1650 cm^{-1} for data in a–h. (k) Fluorescence image of Sheila Flexneri bacteria expressing GFP. (l) Single-frame F-MIP of the same bacteria at 1650 cm^{-1}. (m) F-MIP image of the same field of view with 100 frames average. (n) Fluorescence intensity of the square area in sequentially acquired hot and cold frames.

fluorescence-enhanced and scattering-based MIP imaging in the wide-field mode using *S. aureus* on a silicon substrate as the test bed. Figure 5a–c shows the fluorescence and F-MIP images of individual *S. aureus* with the IR laser tuned to 1650 cm^{-1}. The signal-to-noise ratio for a single bacterium reaches 33 in single-frame F-MIP and 275 after a 100 frames average. Figure 5d–f shows the scattering and SC-MIP images of individual *S. aureus* with the IR laser tuned to 1650 cm^{-1}. Figure 5g and 5h shows the intensity profile across the white line indicated in the images. The Sc-MIP contrast is completely buried in the speckled pattern in singe-frame acquisition. After a 100 frames average, the signal-to-noise ratio reaches 14, which is 20 times lower than that of F-MIP of the same sample. The much higher signal-to-noise ratio in F-MIP can be attributed to the lack of shot noise from scattered photons and the much larger thermosensitivity of the fluorescence probe. Figure 5h shows a similar line width for the bacterium in Sc-MIP and F-MIP. However, the F-MIP intensity does not suffer from the interference (i.e., the dark ring around the peak) encountered in the Sc-MIP image. Figure 5i and 5j shows the F-MIP and Sc-MIP intensities from a single bacterium in sequentially acquired hot and cold frames. The modulation depth, defined as the percentage of intensity difference between hot and cold frames, is found to be about 4% for F-MIP but is buried in frame to frame fluctuations in Sc-MIP. Moreover, Figure 5i shows negligible photobleaching in the recorded 50 frames over a period of 1.25 s.

Besides fluorescent dyes, we tested the feasibility of F-MIP imaging for cells expressing green fluorescent proteins (GFPs). It has been shown that GFPs are highly thermosensitive with a 1% intensity decrease per degree in temperature rise.[47,48] Accordingly, in F-MIP imaging of Sheila Flexneri bacteria expressing GFP (Figure 5k–m), we observed a 2% fluorescence intensity difference between the cold and the hot frames (Figure 5n). The signal-to-noise ratio reaches 10 and 97 in a single frame and a 100 frames average, respectively. The recorded 50 frames only experienced 3% photobleaching.

https://doi.org/10.1021/jacs.1c03642
J. Am. Chem. Soc. 2021, 143, 11490–11499

The fluorescence fluctuation from frame to frame was due to laser instability.

Recently, the Tokmakoff and Min groups reported two related methods that code vibrational signatures into fluorescence spectroscopy based on femtosecond-scale infrared pulse excitation[49] and picosecond-scale stimulated Raman excitation,[50] respectively. These methods are based on the upconversion process in which vibrational excitation and fluorescence emission are from the same dye molecule. Our F-MIP method is fundamentally different in that the fluorescence emission efficiency from a thermosensitive probe is modulated by nanosecond-scale pulsed infrared excitation of the molecules of interest surrounding the probe. We note that the Simpson group independently developed a fluorescence-detected scanning photothermal microscope for chemical imaging of pharmaceutical samples.[51] Their work and the current study show broad applications enabled by F-MIP microscopy.

Photothermal microscopy is a pump−probe technique involving modulation of the pump beam and demodulation of the signal usually by a lock-in. In this work, the sensitivity is defined as the modulation depth, $\Delta I_{pr}/I_{pr} = \sigma I_p$, where σ is related to the thermal sensitivity, I_p is the IR pump, and I_{pr} is the probe intensity. In this sense, fluorescence-detected MIP is more sensitive than scattering-based MIP due to the much larger thermosensitivity of the fluorophores. Experimentally, as shown in Figure 5, the modulation depth in F-MIP is about 2% whereas the modulation is buried in frame-to-frame intensity fluctuation in Sc-MIP. These data are in good agreement with our model.

We defined the imaging SNR as the ratio of signal intensity from single particles to pixel-to-pixel background fluctuations. Thus, in Sc-MIP, the SNR = Signal/(Noise_PD + Noise_photon). In F-MIP, SNR = Signal/Noise_PMT. Under the shot noise limit, the photon noise is proportional to $\sqrt{I_{pr}}$. On the basis of this model, the SNR depends on the value of σ and the probe beam intensity if we assume that the same IR pump beam is used. In scanning MIP microscopy, the probe power (~10 mW) in the scattering mode can be 10 000 times larger than that in the fluorescence mode (~1 μW). In this case, the SNR in Sc-MIP is dominated by the photon noise and the SNR = $\sigma_{sc} I_p \sqrt{I_{pr}}$. In F-MIP, SNR = $\sigma_f I_p I_{pr}$/Noise_PMT. In this case, the SNR in F-MIP is a trade-off between a much larger σ and a much smaller I_{pr} used. Experimentally, we observed a similar SNR in F-MIP compared to Sc-MIP (see Figure 2). However, in wide-field MIP microscopy, limited by the well depth of a common CMOS camera, the probe power at each pixel is at the nW level for both the scattering and the fluorescence modality. In this case, the detector noises dominate and the SNR in F-MIP can be theoretically larger by 2 orders of magnitude than that in Sc-MIP. In the experiment, we showed that the SNR in wide-field MIP is 20 times larger than that in wide-field Sc-MIP.

Theoretically, F-MIP microscopy is based the thermal diffusion from the target molecule to the fluorescent probe. The thermal diffusion length is defined as $\mu_t = 2\sqrt{\alpha t}$, where α is the thermal diffusivity.[51,52] In an aqueous environment, the value of α is 1.4×10^{-7} m^2/s.[53,54] In our wide-field F-MIP experiment, the IR pulse is 900 ns in duration and the fluorescence excitation pulse is 300 nm. If we set the pump−probe delay to be 900 ns, the thermal diffusion length is ~700 nm, which is slightly larger than the diffraction limit of the visible probe beam. If one can use IR pump and visible probe pulses of 5 ns duration and the pump−probe delay is set to be 5 ns, the thermal diffusion length can be reduced to 50 nm. In this case, one can detect the chemical content surrounding the fluorescence probe on the nanoscale. If the probe is conjugated to the target molecule, like a GFP conjugated to a protein, the intramolecular vibrational redistribution on the picosecond scale can be much faster than intermolecular vibrational redistribution. In principle, it could create an intramolecular F-MIP signal, assuming that picosecond IR pump and probe pulses are used.

Researchers have studied the dependence of thermosensitivity on two important environmental factors, salt concentration and viscosity. It was shown that the thermosensitivity is nearly independent of the salt concentration in the 10−100 mM range.[55] Also, it was shown that the PEG BODIPY lifetime in the cells is due to the temperature and independent of changes in viscosity.[56] These data suggest that the fluorophores' thermosensitivity can be used as a reliable readout of the mid-infrared photothermal effect.

F-MIP microscopy opens new opportunities for live-cell chemical imaging. First, F-MIP greatly enhances the specificity of MIP microscopy. To illustrate this advantage, one could normalize the F-MIP signal with the direct fluorescence signal. As shown in Figure S3, the normalized F-MIPs images exhibit a more uniform distribution of the signal arising from proteins in regions labeled by the dyes. In contrast, individual mitochondria are clearly seen in the F-MIP image (Figure 3h) due to enrichment of rhodamine 123 in the mitochondria. Second, by F-MIP spectroscopic imaging of specific organelles (e.g., lipid droplets) specifically labeled by a thermosensitive fluorophore (e.g., BODIPY), one will be able to tell not only the amount and distribution but also the composition of lipids, which is beyond the reach by fluorescence microscopy alone. Such capacity will allow quantitation of lipid metabolism in cells under various conditions (e.g., in response to a stress). Third, F-MIP microscopy opens new ways to push the boundary of mid-infrared photothermal microscopy. For example, integration of infrared laser excitation and light field fluorescence probing is expected to enable single-shot volumetric infrared spectroscopic imaging at a submicrometer spatial resolution. In addition, structured illumination can be harnessed to break the diffraction limit of the visible beam, which is expected to push the spatial resolution of MIP microscopy to a new level.

Compared to MIP microscopy, F-MIP microscopy relies on labeling the specimen with a thermosensitive dye and the signal level depends on the dye concentration. Unlike scattering-based MIP, F-MIP cannot detect vibrational excitation at locations where fluorescent dyes do not exist. When interpreting the F-MIP contrast, one should use the fluorescence image as a reference. For quantitative comparison of the F-MIP signal level between different particles, normalization with fluorescence intensity is needed. An alternative approach is to measure the thermal modulation of the fluorescence lifetime instead of the intensity. For the same reason, the SNR in F-MIP microscopy depends on the number of fluorophores in the particles to be detected. For biological nanoparticles such as virion particles, the small number of fluorescent labels may give a low signal level and limit the SNR accordingly. In such case, detection of interferometric scattering becomes a more suitable approach. In fact, detection

https://doi.org/10.1021/jacs.1c03642
J. Am. Chem. Soc. 2021, 143, 11490−11499

and fingerprinting of single virus particles has been achieved by an interferometric mid-infrared photothermal microscope.[40]

CONCLUSIONS

In efforts to push the detection limit and increase the specificity of optically detected mid-infrared photothermal microscopy, a new platform termed fluorescence-enhanced mid-infrared photothermal (F-MIP) microscopy is developed. Our platform harnesses thermosensitive fluorescent probes to sense the surrounding temperature rise induced by pulsed infrared excitation. High spectral fidelity is demonstrated for fluorescent probes in DMSO solution and inside biological cells. In the point-scanning modality, we demonstrated F-MIP imaging and fingerprinting of a single bacterium. While using fluorescence as a read out, the fingerprint information would allow functional assessment of the biological specimen, such as the metabolic response of bacteria to antibiotics treatment. Furthermore, organelle-specific F-MIP imaging is achieved, which opens exciting opportunities of probing the chemical content of intracellular organelles. In the wide-field modality, we demonstrated the video rate, high signal-to-noise ratio, speckle-free F-MIP imaging of individual bacteria. Finally, our platform is applicable to biological cells expressing GFP. This approach opens new opportunities of monitoring the secondary structure of specific proteins tagged by GFP, which is beyond the reach of IR spectroscopy or fluorescence spectroscopy alone.

ASSOCIATED CONTENT

Supporting Information

The Supporting Information is available free of charge at https://pubs.acs.org/doi/10.1021/jacs.1c03642.

Mid-IR illumination area, spatial resolution of wide-field F-MIP microscopy, and contrast of the F-MIP signals normalized by fluorescence intensity (PDF)

AUTHOR INFORMATION

Corresponding Author

Ji-Xin Cheng − *Department of Physics, Department of Electrical and Computer Engineering, Department of Biomedical Engineering, and Photonics Center, Boston University, Boston, Massachusetts 02215, United States;* orcid.org/0000-0002-5607-6683; Email: jxcheng@bu.edu

Authors

Yi Zhang − *Department of Physics, Boston University, Boston, Massachusetts 02215, United States*

Haonan Zong − *Department of Electrical and Computer Engineering, Boston University, Boston, Massachusetts 02215, United States*

Cheng Zong − *Department of Electrical and Computer Engineering, Boston University, Boston, Massachusetts 02215, United States*

Yuying Tan − *Department of Biomedical Engineering, Boston University, Boston, Massachusetts 02215, United States*

Meng Zhang − *Department of Electrical and Computer Engineering, Boston University, Boston, Massachusetts 02215, United States*

Yuewei Zhan − *Department of Biomedical Engineering, Boston University, Boston, Massachusetts 02215, United States*

Complete contact information is available at: https://pubs.acs.org/10.1021/jacs.1c03642

Author Contributions

[§]Y.Z. and H.Z.: These authors contributed equally.

Notes

The authors declare no competing financial interest.

ACKNOWLEDGMENTS

This work was supported by R35GM136223 and R43GM142346 to J.X.C.

REFERENCES

(1) Gonçalves, M. S. T. Fluorescent labeling of biomolecules with organic probes. *Chem. Rev.* **2009**, *109* (1), 190−212.

(2) Dean, K. M.; Palmer, A. E. Advances in fluorescence labeling strategies for dynamic cellular imaging. *Nat. Chem. Biol.* **2014**, *10* (7), 512−523.

(3) Rust, M. J.; Bates, M.; Zhuang, X. Sub-diffraction-limit imaging by stochastic optical reconstruction microscopy (STORM). *Nat. Methods* **2006**, *3* (10), 793−796.

(4) Gustafsson, M. G. Surpassing the lateral resolution limit by a factor of two using structured illumination microscopy. *J. Microsc.* **2000**, *198* (2), 82−87.

(5) Shroff, H.; Galbraith, C. G.; Galbraith, J. A.; Betzig, E. Live-cell photoactivated localization microscopy of nanoscale adhesion dynamics. *Nat. Methods* **2008**, *5* (5), 417−423.

(6) Moschou, E. A.; Sharma, B. V.; Deo, S. K.; Daunert, S. Fluorescence glucose detection: advances toward the ideal in vivo biosensor. *J. Fluoresc.* **2004**, *14* (5), 535−547.

(7) Mukherjee, S.; Zha, X.; Tabas, I.; Maxfield, F. R. Cholesterol distribution in living cells: fluorescence imaging using dehydroergosterol as a fluorescent cholesterol analog. *Biophys. J.* **1998**, *75* (4), 1915−1925.

(8) Cheng, J.-X.; Xie, X. S. Vibrational spectroscopic imaging of living systems: An emerging platform for biology and medicine. *Science* **2015**, *350* (6264), aaa8870.

(9) Cheng, J.-X.; Xie, X. S. Coherent anti-Stokes Raman scattering microscopy: instrumentation, theory, and applications. *J. Phys. Chem. B* **2004**, *108* (3), 827−840.

(10) Hu, F.; Shi, L.; Min, W. Biological imaging of chemical bonds by stimulated Raman scattering microscopy. *Nat. Methods* **2019**, *16* (9), 830−842.

(11) Liao, C.-S.; Slipchenko, M. N.; Wang, P.; Li, J.; Lee, S.-Y.; Oglesbee, R. A.; Cheng, J.-X. Microsecond scale vibrational spectroscopic imaging by multiplex stimulated Raman scattering microscopy. *Light: Sci. Appl.* **2015**, *4* (3), e265−e265.

(12) Yue, S.; Li, J.; Lee, S.-Y.; Lee, H. J.; Shao, T.; Song, B.; Cheng, L.; Masterson, T. A.; Liu, X.; Ratliff, T. L.; et al. Cholesteryl ester accumulation induced by PTEN loss and PI3K/AKT activation underlies human prostate cancer aggressiveness. *Cell Metab.* **2014**, *19* (3), 393−406.

(13) Li, J.; Condello, S.; Thomes-Pepin, J.; Ma, X.; Xia, Y.; Hurley, T. D.; Matei, D.; Cheng, J.-X. Lipid desaturation is a metabolic marker and therapeutic target of ovarian cancer stem cells. *Cell Stem Cell* **2017**, *20* (3), 303−314.

(14) Du, J.; Su, Y.; Qian, C.; Yuan, D.; Miao, K.; Lee, D.; Ng, A. H.; Wijker, R. S.; Ribas, A.; Levine, R. D.; et al. Raman-guided subcellular pharmaco-metabolomics for metastatic melanoma cells. *Nat. Commun.* **2020**, *11* (1), 14830.

(15) Fernandez, D. C.; Bhargava, R.; Hewitt, S. M.; Levin, I. W. Infrared spectroscopic imaging for histopathologic recognition. *Nat. Biotechnol.* **2005**, *23* (4), 469−474.

(16) Findlay, C.; Wiens, R.; Rak, M.; Sedlmair, J.; Hirschmugl, C.; Morrison, J.; Mundy, C.; Kansiz, M.; Gough, K. Rapid biodiagnostic ex vivo imaging at 1 μm pixel resolution with thermal source FTIR FPA. *Analyst* **2015**, *140* (7), 2493−2503.

(17) Kazarian, S. G.; Chan, K. A. ATR-FTIR spectroscopic imaging: recent advances and applications to biological systems. *Analyst* **2013**, *138* (7), 1940−1951.
(18) Lasch, P.; Haensch, W.; Naumann, D.; Diem, M. Imaging of colorectal adenocarcinoma using FT-IR microspectroscopy and cluster analysis. *Biochim. Biophys. Acta, Mol. Basis Dis.* **2004**, *1688* (2), 176−186.
(19) Sattlecker, M.; Baker, R.; Stone, N.; Bessant, C. Support vector machine ensembles for breast cancer type prediction from mid-FTIR micro-calcification spectra. *Chemom. Intell. Lab. Syst.* **2011**, *107* (2), 363−370.
(20) Tang, J.; Luan, F.; Chen, X. Binding analysis of glycyrrhetinic acid to human serum albumin: Fluorescence spectroscopy, FTIR, and molecular modeling. *Bioorg. Med. Chem.* **2006**, *14* (9), 3210−3217.
(21) Miller, L. M.; Bourassa, M. W.; Smith, R. J. FTIR spectroscopic imaging of protein aggregation in living cells. *Biochim. Biophys. Acta, Biomembr.* **2013**, *1828* (10), 2339−2346.
(22) Zlotogorski-Hurvitz, A.; Dekel, B. Z.; Malonek, D.; Yahalom, R.; Vered, M. FTIR-based spectrum of salivary exosomes coupled with computational-aided discriminating analysis in the diagnosis of oral cancer. *J. Cancer Res. Clin. Oncol.* **2019**, *145* (3), 685−694.
(23) Zhang, D.; Li, C.; Zhang, C.; Slipchenko, M. N.; Eakins, G.; Cheng, J.-X. Depth-resolved mid-infrared photothermal imaging of living cells and organisms with submicrometer spatial resolution. *Science Advances* **2016**, *2* (9), e1600521.
(24) Li, Z.; Aleshire, K.; Kuno, M.; Hartland, G. V. Super-resolution far-field infrared imaging by photothermal heterodyne imaging. *J. Phys. Chem. B* **2017**, *121* (37), 8838−8846.
(25) Li, C.; Zhang, D.; Slipchenko, M. N.; Cheng, J.-X. Mid-infrared photothermal imaging of active pharmaceutical ingredients at submicrometer spatial resolution. *Anal. Chem.* **2017**, *89* (9), 4863−4867.
(26) Bai, Y.; Zhang, D.; Li, C.; Liu, C.; Cheng, J.-X. Bond-selective imaging of cells by mid-infrared photothermal microscopy in high wavenumber region. *J. Phys. Chem. B* **2017**, *121* (44), 10249−10255.
(27) Li, X.; Zhang, D.; Bai, Y.; Wang, W.; Liang, J.; Cheng, J.-X. Fingerprinting a living cell by Raman integrated mid-infrared photothermal microscopy. *Anal. Chem.* **2019**, *91* (16), 10750−10756.
(28) Lim, J. M.; Park, C.; Park, J.-S.; Kim, C.; Chon, B.; Cho, M. Cytoplasmic protein imaging with mid-infrared photothermal microscopy: cellular dynamics of live neurons and oligodendrocytes. *J. Phys. Chem. Lett.* **2019**, *10* (11), 2857−2861.
(29) Shi, J.; Wong, T. T.; He, Y.; Li, L.; Zhang, R.; Yung, C. S.; Hwang, J.; Maslov, K.; Wang, L. V. High-resolution, high-contrast mid-infrared imaging of fresh biological samples with ultraviolet-localized photoacoustic microscopy. *Nat. Photonics* **2019**, *13* (9), 609−615.
(30) Pavlovetc, I. M.; Podshivaylov, E. A.; Chatterjee, R.; Hartland, G. V.; Frantsuzov, P. A.; Kuno, M. Infrared photothermal heterodyne imaging: Contrast mechanism and detection limits. *J. Appl. Phys.* **2020**, *127* (16), 165101.
(31) Bai, Y.; Yin, J.; Cheng, J.-X. Bond-Selective Imaging by Optically Sensing the Mid-Infrared Photothermal Effect. *Science Advances* **2021**, *7* (20), eabg1559.
(32) Zhang, D.; Lan, L.; Bai, Y.; Majeed, H.; Kandel, M. E.; Popescu, G.; Cheng, J.-X. Bond-selective transient phase imaging via sensing of the infrared photothermal effect. *Light: Sci. Appl.* **2019**, *8* (1), 116.
(33) Bai, Y.; Zhang, D.; Lan, L.; Huang, Y.; Maize, K.; Shakouri, A.; Cheng, J.-X. Ultrafast chemical imaging by widefield photothermal sensing of infrared absorption. *Science Advances* **2019**, *5* (7), eaav7127.
(34) Schnell, M.; Mittal, S.; Falahkheirkhah, K.; Mittal, A.; Yeh, K.; Kenkel, S.; Kajdacsy-Balla, A.; Carney, P. S.; Bhargava, R. All-digital histopathology by infrared-optical hybrid microscopy. *Proc. Natl. Acad. Sci. U. S. A.* **2020**, *117* (7), 3388−3396.
(35) Tamamitsu, M.; Toda, K.; Shimada, H.; Honda, T.; Takarada, M.; Okabe, K.; Nagashima, Y.; Horisaki, R.; Ideguchi, T. Label-free biochemical quantitative phase imaging with mid-infrared photothermal effect. *Optica* **2020**, *7* (4), 359−366.
(36) Xu, J.; Li, X.; Guo, Z.; Huang, W. E.; Cheng, J.-X. Fingerprinting Bacterial Metabolic Response to Erythromycin by Raman-Integrated Mid-Infrared Photothermal Microscopy. *Anal. Chem.* **2020**, *92* (21), 14459−14465.
(37) Marcott, C.; Kansiz, M.; Dillon, E.; Cook, D.; Mang, M. N.; Noda, I. Two-dimensional correlation analysis of highly spatially resolved simultaneous IR and Raman spectral imaging of bioplastics composite using optical photothermal Infrared and Raman spectroscopy. *J. Mol. Struct.* **2020**, *1210*, 128045.
(38) Klementieva, O.; Sandt, C.; Martinsson, I.; Kansiz, M.; Gouras, G. K.; Borondics, F. Super-Resolution Infrared Imaging of Polymorphic Amyloid Aggregates Directly in Neurons. *Advanced Science* **2020**, *7* (6), 1903004.
(39) Banas, A.; Banas, K.; Lo, M. K. F.; Kansiz, M.; Kalaiselvi, S. M. P.; Lim, S. K.; Loke, J.; Breese, M. B. H. Detection of High-Explosive Materials within Fingerprints by Means of Optical-Photothermal Infrared Spectromicroscopy. *Anal. Chem.* **2020**, *92* (14), 9649−9657.
(40) Zhang, Y.; Yurdakul, C.; Devaux, A. J.; Wang, L.; Xu, X. G.; Connor, J. H.; Ünlü, M. S.; Cheng, J.-X. Vibrational Spectroscopic Detection of a Single Virus by Mid-Infrared Photothermal Microscopy. *Anal. Chem.* **2021**, *93* (8), 4100−4107.
(41) Grabowski, Z. R.; Rotkiewicz, K.; Rettig, W. Structural changes accompanying intramolecular electron transfer: focus on twisted intramolecular charge-transfer states and structures. *Chem. Rev.* **2003**, *103* (10), 3899−4032.
(42) Chen, Y. Y.; Wood, A. W. Application of a temperature-dependent fluorescent dye (Rhodamine B) to the measurement of radiofrequency radiation-induced temperature changes in biological samples. *Bioelectromagnetics* **2009**, *30* (7), 583−590.
(43) Gosse, C.; Bergaud, C.; Löw, P. Molecular probes for thermometry in microfluidic devices. *Top. Appl. Phys.* **2009**, *118*, 301−341.
(44) Maksimov, E. G.; Yaroshevich, I. A.; Tsoraev, G. V.; Sluchanko, N. N.; Slutskaya, E. A.; Shamborant, O. G.; Bobik, T. V.; Friedrich, T.; Stepanov, A. V. A genetically encoded fluorescent temperature sensor derived from the photoactive Orange Carotenoid Protein. *Sci. Rep.* **2019**, *9* (1), 8937.
(45) Greenspan, P.; Mayer, E. P.; Fowler, S. D. Nile red: a selective fluorescent stain for intracellular lipid droplets. *J. Cell Biol.* **1985**, *100* (3), 965−973.
(46) Baracca, A.; Sgarbi, G.; Solaini, G.; Lenaz, G. Rhodamine 123 as a probe of mitochondrial membrane potential: evaluation of proton flux through F0 during ATP synthesis. *Biochim. Biophys. Acta, Bioenerg.* **2003**, *1606* (1−3), 137−146.
(47) Zhang, C.; Liu, M.-S.; Xing, X.-H. Temperature influence on fluorescence intensity and enzyme activity of the fusion protein of GFP and hyperthermophilic xylanase. *Appl. Microbiol. Biotechnol.* **2009**, *84* (3), 511−517.
(48) Donner, J. S.; Thompson, S. A.; Kreuzer, M. P.; Baffou, G.; Quidant, R. Mapping intracellular temperature using green fluorescent protein. *Nano Lett.* **2012**, *12* (4), 2107−2111.
(49) Whaley-Mayda, L.; Penwell, S. B.; Tokmakoff, A. Fluorescence-Encoded Infrared Spectroscopy: Ultrafast Vibrational Spectroscopy on Small Ensembles of Molecules in Solution. *J. Phys. Chem. Lett.* **2019**, *10* (8), 1967−1972.
(50) Xiong, H.; Shi, L.; Wei, L.; Shen, Y.; Long, R.; Zhao, Z.; Min, W. Stimulated Raman excited fluorescence spectroscopy and imaging. *Nat. Photonics* **2019**, *13* (6), 412−417.
(51) Li, M.; Razumtcev, A.; Yang, R.; Liu, Y.; Rong, J.; Geiger, A. C.; Blanchard, R.; Pfluegl, C.; Taylor, L. S.; Simpson, G. J. Fluorescence-detected mid-infrared photothermal microscopy. *arXiv:2104.02900* **2021**, https://arxiv.org/abs/2104.0290 (accessed 29 Jun 2021).
(52) Lienhard, I.; John, H. *A heat transfer textbook*; Phlogiston Press, 2005.
(53) Marín, E. Characteristic dimensions for heat transfer. *Lat.-Am. J. Phys. Educ.* **2010**, *4* (1), 56−60.
(54) James, D. The thermal diffusivity of ice and water between −40 and + 60° C. *J. Mater. Sci.* **1968**, *3* (5), 540−543.

(55) Liu, W. T.; Wu, J. H.; Li, E. S.; Selamat, E. S. Emission characteristics of fluorescent labels with respect to temperature changes and subsequent effects on DNA microchip studies. *Appl. Environ. Microbiol.* **2005**, *71* (10), 6453−7.
(56) Ogle, M. M.; Smith McWilliams, A. D.; Ware, M. J.; Curley, S. A.; Corr, S. J.; Martí, A. A. Sensing temperature in vitro and in cells using a BODIPY molecular probe. *J. Phys. Chem. B* **2019**, *123* (34), 7282−7289.

https://doi.org/10.1021/jacs.1c03642
J. Am. Chem. Soc. 2021, 143, 11490−11499